J Mater Sci (2009) 44:4140–4147
DOI 10.1007/s10853-009-3607-4

Determination of mechanical properties of Al–Mg alloys dissimilar friction stir welded interface by indentation methods

P. Venkateswaran · Zhi-Hui Xu · Xiaodong Li · A. P. Reynolds

Received: 10 March 2009 / Accepted: 14 May 2009 / Published online: 2 June 2009

Abstract A series of friction stir welds was produced between heat treated Al–Mg–Si and strain hardened Mg–Al–Zn alloy sheets. Weld evaluation by transverse tensile testing showed a wide range of strengths and all the failures occurred along the weld interface. The formation of intermetallic compounds in the weld joints was investigated by X-ray diffraction, scanning electron microscopy imaging, and elemental analysis techniques. Micro and nanoindentation characterization methods were used to evaluate the mechanical properties at the interface, including the fracture toughness. The fracture toughness measurements by a Vickers indenter introduced Palmqvist type cracks at all four corners of the indents and cube corner indenter resulted in the intermetallic chipping. The fracture toughness (K_{IC}) calculation by both the micro and nanoindentation methods showed very low values, which is the primary reason for the brittle failure of the dissimilar weld joints and concomitant low tensile strengths.

Introduction

Friction stir welding (FSW) is a solid state welding process invented in 1991 by The Welding Institute, UK [1]. Since, its invention, many research results explaining the experimental and simulation aspects on the FSW of aluminum [1–5] and magnesium alloys [6–9] have been published. The FSW process is a proven manufacturing method for joining of hard to weld materials, like Al, Mg etc. with relatively better weld quality compared to the conventional fusion welding processes [1–9]. In certain applications, it might be advantageous to join dissimilar Al alloys (e.g., cast to wrought Al) and Mg alloys, which may give the combined benefits of both the alloys. The solid state nature of the FSW makes this process attractive for producing dissimilar Al alloy [10] and Al to Mg alloy weld joints [11], which are difficult to weld by the conventional fusion welding processes. This is because the former process avoids melting related defects that are commonly observed in the fusion welding processes. However, the formation of the Al–Mg intermetallic compounds at the interface and surrounding regions is inevitable in welding aluminum alloys to magnesium alloys, regardless of the welding processes. Recent reports of FSW lap [12] and butt joints [13] between Al alloys and Mg alloys indicate that the interface invariably contains an intermetallic layer that is several micrometers thick, and the weld joints are very brittle. The compound layer interface has also been reported on steel–Al [14] and Mg–Cu dissimilar fusion welds [15]. The effect of intermetallic layer thickness on steel–Al laser welded joints strength has been reported by Borrisutthekul et al. [14]. McLean et al. [13] have reported the melting of the Al–Mg intermetallic phase during the FSW process and the failure of the weld joints by debonding of the intermetallic layer at the interface from the adjacent Al base metal. Similarly, the spontaneous melting of the intermetallic phases was reported by Gerlich et al. [16] on various aluminum alloys and Al–Mg dissimilar Friction Stir spot welds [17]. These results indicate that the mechanical properties of the dissimilar materials weld joints are influenced by the intermetallic phases at the interface. Therefore, detailed knowledge regarding the

P. Venkateswaran · Z.-H. Xu · X. Li · A. P. Reynolds (✉)
Department of Mechanical Engineering, University of South Carolina, 300 Main Street, Columbia, SC 29208, USA
e-mail: reynolds@cec.sc.edu

P. Venkateswaran
e-mail: venkatep@engr.sc.edu

intermetallic layer properties including the fracture behavior would be essential to explain the overall dissimilar weld joint properties. However, the narrowness of the intermetallic layer makes conventional mechanical property evaluation methods unsuitable for precise determination of the interface properties. For example, the use of microindentation method to measure the properties of the interface, which is much smaller than a typical indent size, would result in underestimation of the intermetallic layer properties, e.g., the measured Vickers hardness would be the combined hardness of the intermetallic and adjacent base materials. However, research focusing on the mechanical properties of the narrow, intermetallic layer of the dissimilar weld joints is limited: only the microhardness of the layer has been characterized [18, 19] on the Al–Mg weld joints. Considering these aspects, the aim of the present study is to characterize the narrow interface of the Al–Mg welded interface for the intermetallic phases, mechanical properties including the fracture toughness by sub-micron scale property evaluation methods such as nanoindentation. The measured properties by nanoindentation method have been compared with microindentation results and were used to explain the overall weld joint strength and its fracture behavior.

In brittle materials radial cracks are generated during the nanoindentation and the known crack length is used to calculate the fracture toughness. Low toughness ceramics and glasses exhibit fragmentation and chipping [20], when loaded by sharp indenters. In this case, the crack length is not known, and the calculation of fracture toughness based on the crack length is not applicable. Li and Bhushan [21] have proposed a method to calculate K_{IC} from the energy release rate during cracking by calculating the projected area of the step in the load–displacement curve of thin films. Chai and Lawn [22] have conducted the edge chipping tests on monolithic brittle materials, and used the chipping load and indentation location relative to the front face to calculate the fracture toughness. In this article, the fracture toughness of the intermetallic layer at the 6063 Al and AZ31B Mg FSW joints was calculated from the load to cause chipping and the chip size resulting from a cube corner indenter.

Experimental procedures

The base materials used for the friction stir butt weld joints are 3.25 mm thick sheets of 6063-T5 (Al–0.7 wt% Mg–0.4 wt% Si) aluminum and AZ31B-H24 (Mg–3 wt% Al–1 wt% Zn) magnesium alloys. The joints were produced using an MTS Friction Stir Welding Machine with a tool having 18 mm diameter flat edge concave shoulder (H13 tool steel) and 5 mm diameter probe made of MP159 (cobalt base alloy), with a tool tilt angle of 3° from vertical. The parameters used for the welding are in the following ranges; tool rotational speed of 900–2700 rpm, welding speed of 1.7–6.4 mm s^{-1} and the z-force of 2.5–17.2 kN. The Friction Stir Weld joints were processed with the Al on the advancing side with the initial interface positioned in the weld centerline. Temperature during welding was measured using a k-type thermocouple spot welded inside the probe at approximately the midplane of the sheet with a data acquisition frequency of 1 Hz. Tensile testing was performed using an MTS servo hydraulic system with a displacement rate of 0.025 mm min^{-1}. An extensometer of 25 mm gauge length was used for the strain measurement during tensile testing. Transverse tensile tests of the weld joints were performed on flat, pin loaded, specimens of dimensions 12.5 mm wide × 150 mm long. Base materials tensile properties were evaluated using flat, dog bone shaped specimens as per ASTM E8-04 [23].

Cross sections for microstructural and indentation tests were cut by a high velocity water jet. The cross sections were epoxy mounted for metallography and microhardness tests. For nanoindentation measurements, the cross sections were used without epoxy mounting. The cross sections of the weld joint were polished with silicon carbide abrasive papers followed by 5 and 3 μm alumina powders and, finally, 0.3 μm colloidal silica. The Al side of the weld joint was etched using 85% water, 10% sulfuric acid, and 5% hydrofluoric acid solution for 30 s. The Mg side of the weld joint was etched using 14 mL picric acid, 2 mL glacial acetic acid, and 2 mL water solution for 5 s. An Olympus optical microscope was used for low magnification microstructural examination. An FEI Quanta 200 ESEM and Hitachi S4800 FESEM scanning electron microscope (SEM) equipped with an energy dispersive X-ray analysis systems were used for higher magnification microstructural examination and for determination of the composition in and around the weld interface.

Vickers hardness testing across the weld interface was performed using a Beuhler Micromet-1 microhardness tester (Buehler Ltd, Lake Bluff, Illinois, USA) with loads of 0.1 N (near the interface) and 1 N (other than interface locations) and with 10 s loading time. The Vickers hardness profile was obtained at the mid-plane of the weld joint cross section. Knoop hardness indentation was performed with the long edge of the indenter placed parallel to the interface so as to minimize the indent dimension perpendicular to the interface. The indentation load and loading time are 0.1 N and 10 s, respectively. Nanoindentations were performed across and at the interface of the as-welded Al–Mg joint using a Triboscope (Hysitron Inc. Minneapolis, MN, USA) in conjunction with a Veeco Dimension 3100 AFM system (Veeco Metrology Group, Woodbury, New York, USA). A well-calibrated Berkovich indenter

was used for the measurement of elastic modulus and hardness. A constant peak indentation force of 0.8 mN was used for all the indentations and the peak indentation force reaches its maximum in 5 s and is then removed in the same time after a 5-s hold at the peak force. The hardness and elastic modulus were determined from the load–penetration depth curve of the indentation using the method of Oliver and Pharr [24]. The hardness is given by

$$H = \frac{P_{\max}}{A_c} \tag{1}$$

where, $P_{\max}$ is the peak indentation load, A_c is the projected contact area. The elastic modulus is calculated using the following equations:

$$E_r = \frac{\sqrt{\pi}}{2} \cdot \frac{S}{\sqrt{A_c}} \tag{2}$$

$$\frac{1}{E_r} = \frac{1 - v_i^2}{E_i} + \frac{1 - v_s^2}{E_s} \tag{3}$$

where E_r is the reduced modulus, S is the contact stiffness determined from the unloading curve, E_i, E_s, v_i, and v_s are the elastic moduli and Poisson's ratios of the indenter and specimen, where $E_i = 1040$ GPa, $v_i = 0.07$ for the diamond indenter. The nanoindentation fracture toughness measurements were performed on the as-welded Al–Mg interface using a sharp cube corner indenter with four different loads, 1, 1.5, 2, and 2.5 mN for 5 s.

Vickers microindentation fracture toughness measurements were performed on post-weld heat treated Al–Mg weld interfaces. A post-weld heat treatment of 673 K for 20 min was employed to increase the intermetallic thickness to enable microindentation within the intermetallic layer. Several Vickers indentations were made at the intermetallic layer using a 1 N load for 10 s. XRD analysis was performed on powders ground from the transverse tensile fracture surfaces using a Rigaku DMax 2100 diffractometer with monochromatic Cu-K_α radiation, 36 mA current, and a voltage of 36 kV.

Results and discussion

Optical microscopy of the weld cross section

Figure 1 shows the etched macrograph of a dissimilar weld joint cross section with Al and Mg on the advancing and retreating sides, respectively. The cross section shows an interpenetrating feature (an inverted airfoil shaped object) extended more towards the advancing side (Al) and less on the retreating side (Mg) of the weld joint and an inclined weld interface on the top and bottom of the interpenetrating feature. A complex weld interface with an interpenetrating feature is commonly observed in the dissimilar Friction Stir weld joints, where mixing of both Al and Mg takes place [11, 18]. The complex interface shape was also reported in 5052 and 6061 aluminum alloys Friction Stir lap welds [10]. The occurrence of interpenetrating feature is presumed to be due to the differences in the flow behavior of the base materials.

Knoop and Vickers hardness

Figure 2 shows a very thin continuous intermetallic layer along the interface and a series of Knoop indents across the dissimilar Al–Mg weld interface. Knoop indents (Fig. 2) were obtained at the linear part of the weld interface within 100 μm distance from either side of the weld interface, marked by the square box above the interpenetrating feature shown in Fig. 1. The width of the intermetallic layer was in the range of 1.7–3.5 μm and observed over the entire length of the interface. The maximum temperature observed during FSW was 726 K, close to the aluminum rich eutectic temperature (723 K) in the Al–Mg system and

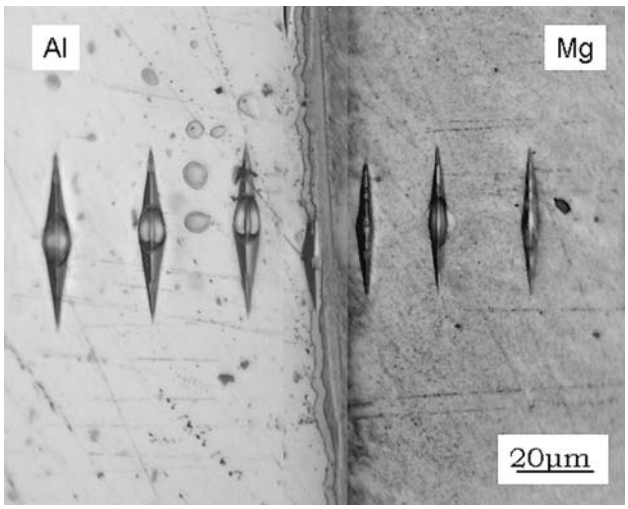

Fig. 2 Optical micrograph of the Al–Mg interface showing an intermetallic layer and Knoop indents

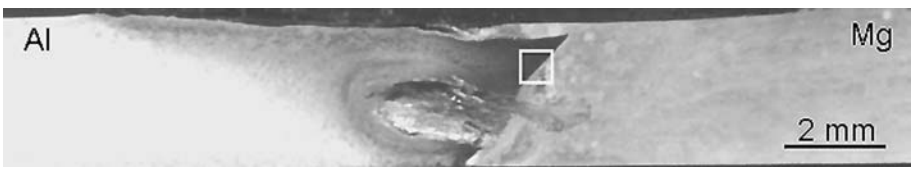

Fig. 1 Cross section of the Al–Mg weld joint. Al on the advancing side and Mg on the retreating side of the weld

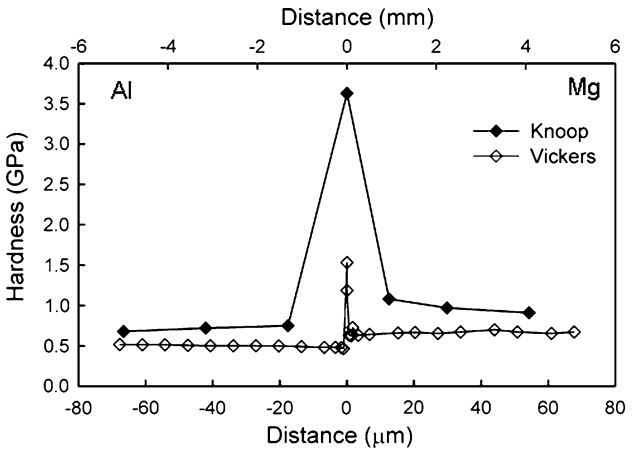

Fig. 3 Vickers and Knoop microhardness profiles across the weld interface showing the maximum hardness at the weld interface

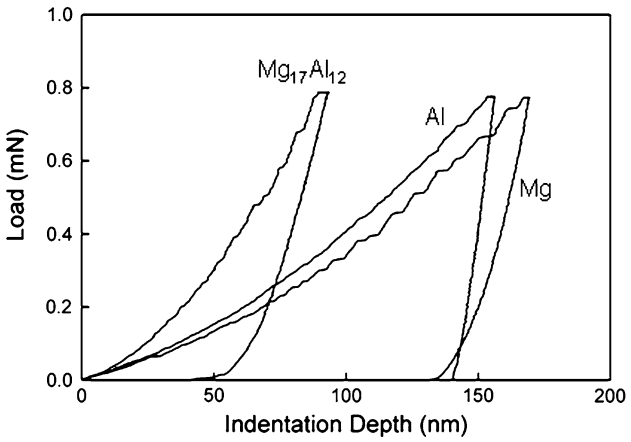

Fig. 4 Berkovich indenter generated load and indentation depth curves for the intermetallic phase and the base materials

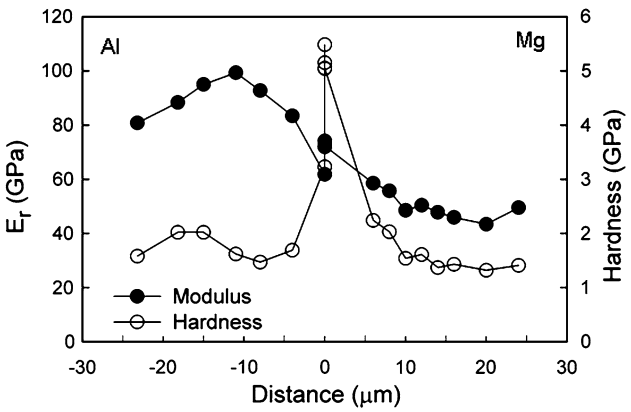

Fig. 5 Hardness and reduced modulus (E_r) profiles across the weld interface measured using Berkovich indenter

significantly above the magnesium rich eutectic temperature of 710 K, indicating that a molten intermetallic was likely present during the FSW process and solidified as divorced eutectic during the weld cooling cycle [13]. The temperature gradient across the sheet thickness caused the thickness variation in the intermetallic layer. The local melting of the intermetallic layer was also reported in Friction Stir spot welds of Al and dissimilar Al–Mg alloys [16, 17].

Figure 3 shows the hardness profile across the Al–Mg weld joint interface obtained by the microhardness testing methods. The maximum hardness was determined at weld interface; 1.56, 3.63 GPa, respectively by Vickers and Knoop hardness testing methods. The hardness at the interface is higher than the rest of the zones (e.g. weld nugget, HAZ etc) in the weld joint. Figure 2 shows the indent size at the intermetallic layer resulting from Knoop hardness test method is larger than the width of the interface (a small part extended into the Al side). Similarly, the indent size resulting from the Vickers method is also larger than the thickness of the intermetallic layer for the smallest load attainable with the microhardness tester; hence, the measured hardness at the interface is the combined hardness of the intermetallic layer at the interface and the matrix materials.

Nanoindentation hardness

Figure 4 shows the load–indentation depth curves obtained using a Berkovich indenter from the nanoindentation test for the Al–Mg weld interface. The indentation depths for the base materials, (6063 and AZ31) and the intermetallic at the interface are 156–169 and 92–93 nm, respectively. Figure 5 shows the hardness and reduced modulus plots across the weld interface. The reduced modulus is a combination of elastic properties of the indenter and the test material, which is defined in Eq. 3 of "Experimental procedures". In Fig. 5, the distance '0' represents the weld centerline, left and right sides of the centerline represent, the Al and Mg base materials, respectively. The highest hardness value observed is 5.18 GPa (average of four measurements): this value was measured in the interface region (zero position). Figure 6 shows the secondary electron SEM image of the nanoindents produced by the Berkovich indenter at and across the weld interface of the location indicated by a square box in Fig. 1. The maximum hardness at the interface is due to the presence of intermetallic compounds, confirmed by EDS analysis. The Al–Mg phase diagram has the following intermediate phases; Mg_2Al_3 (denoted β) is cubic, and $Mg_{17}Al_{12}$ (α Mn-type cubic, denoted γ).The indents 5–8 in Fig. 6 (oriented along the interface) show a composition range of 47–49 at.% Al, which is near the equilibrium composition range (39.5–55 at.% Al) for $Mg_{17}Al_{12}$ type intermetallic as per the Al–Mg phase diagram [25]. The average elastic

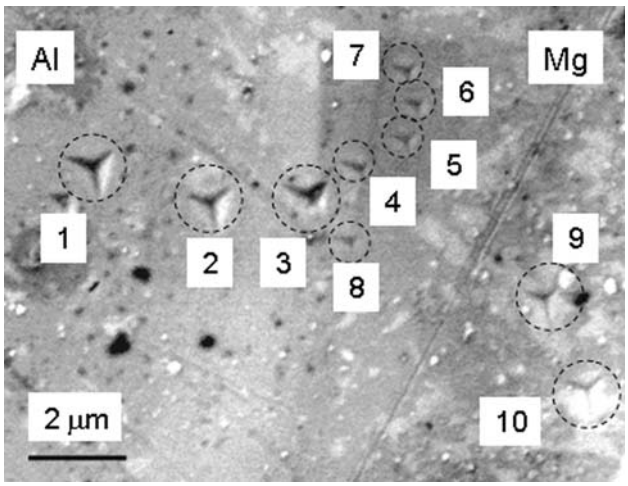

Fig. 6 Secondary electron SEM image of the Berkovich indents at the interface and surrounding areas

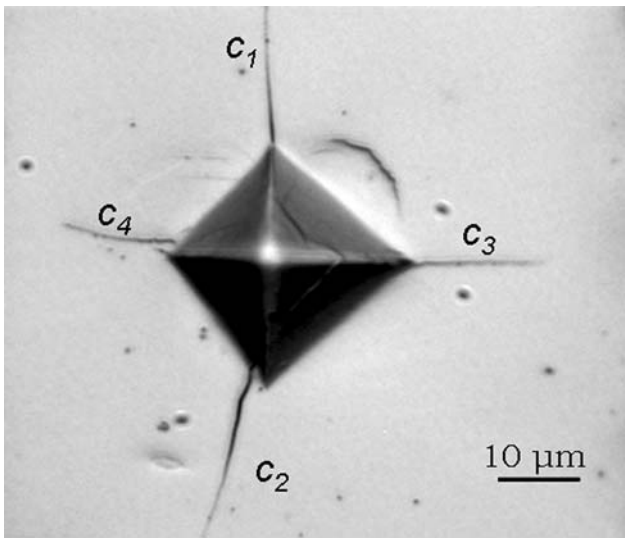

Fig. 7 Optical micrograph showing the cracks at all four corners of a Vickers indent on the post-weld heat treated intermetallic layer

Table 1 Elemental composition (at.%) of nanoindented locations in Fig. 6

Indent number	Al	Mg	Hardness (GPa)	Phase
1	97.27	2.73	1.47	Matrix
2	84.58	15.42	1.69	–
3	36.23	63.77	3.23	–
4	54.68	45.32	3.68	–
5	47.29	52.71	5.04	$Mg_{17}Al_{12}$
6	47.48	52.52	5.48	$Mg_{17}Al_{12}$
7	43.5	55.83	5.15	$Mg_{17}Al_{12}$
8	48.98	50.44	5.05	$Mg_{17}Al_{12}$
9	22.24	77.76	2.24	–
10	5.16	94.84	1.54	Matrix

modulus of the intermetallic layer corresponding to indents 5–8 in Fig. 6 is determined to be 71 GPa, comparable to the values reported in the literature for Al–Mg type intermetallics [26]. The base material hardness values (corresponding to the points far away from the interface in Fig. 5) are 1.58 and 1.41 GPa, respectively, for the Al and Mg alloys. Table 1 gives the chemical composition measured by EDS analysis and the nanoindentation hardness corresponding to the indents shown in Fig. 6.

Microindentation fracture toughness

Figure 7 is an optical micrograph (OM) of the post-weld heat treated Al–Mg weld interface showing the cracks at the corners of a Vickers indent. The post-weld heat treatment resulted in the growth of the intermetallic layer to 75 μm, which enabled the cracks induced by the Vickers indenter to be within the intermetallic layer. The cracks oriented perpendicular to the interface are shorter than those parallel to the interface due, most likely, to the constraint from the adjacent base materials. The fracture toughness was calculated using the following relation [21, 27]

$$K_{IC} = \alpha \left(\frac{E}{H}\right)^{1/2} \left(\frac{P}{c^{3/2}}\right) \quad (4)$$

where α is an empirical constant depending on the geometry of the indenter, E and H are hardness and elastic modulus, and P is the peak indentation load. For Vickers indenters, α was empirically found based on experimental data and is equal to 0.016. H was determined by Vickers indenter on the post-weld heat treated intermetallic layer at a load of 0.1 N (2.6 GPa). The value of E was obtained from the nanoindentation data (71 GPa). The crack length c was measured from the center of the indent to the end of crack using optical micrographs. Assuming that the fracture toughness of the weld joint to be determined, when it is tensile loaded in the direction normal to the weld interface (mode I). In this case cracks, $c1$ and $c2$ parallel to the interface are more important than the lateral cracks, $c3$ and $c4$ in Fig. 7. K_{IC} of the intermetallic layer calculated using the average length of the cracks $c1$ and $c2$ is 0.37 ± 0.07 MPa $m^{1/2}$. The value is marginally higher, when the average length of the cracks ($c1$, $c2$, $c3$, $c4$ in Fig. 7) at all four corners of the indents is substituted in Eq. 4. The fracture toughness was calculated using the crack length data from seven microindents. Often, the hardness value determined by the nanoindentation method is used to determine the microindentation fracture toughness

Table 2 Microindentation fracture toughness values of the intermetallic layer for Vickers and nanoindentation hardness values and different crack lengths

Hardness	Fracture toughness (MPa $m^{1/2}$)	
	Crack lengths parallel to the interface	Average length of the cracks at all four corners
Vickers (2.6 GPa)	0.37 ± 0.07	0.53 ± 0.20
Nanoindentation (5.18 GPa)	0.27 ± 0.05	0.38 ± 0.14

[27]. If the nanoindentation determined hardness (5.18 GPa) is substituted in Eq. 4, K_{IC} values are lower than those calculated using the microhardness value. The microindentation K_{IC} values calculated using Vickers and nanoindentation hardness values are presented in Table 2. The difference in K_{IC} values arises due to the variation in the crack lengths measured parallel and perpendicular to the intermetallic interface layer and the difference in the hardness values determined by micro and nanoindentation methods.

Nanoindentation fracture toughness

Figure 8 shows the load–indentation depth curves of the intermetallic layer obtained from the cube corner indenter for four different loads, 1, 1.5, 2, and 2.5 mN . The load–displacement curves for all the applied loads show many discontinuities, where a sudden increase in the displacement is seen in the loading phase without any appreciable change in the load. This phenomenon is called "pop-in" behavior, noticed in many brittle thin films due to the cracking and chipping events [21, 28]. The SEM micrographs (Fig. 9) of the nanoindents corresponding to the load–indentation depth curves presented in Fig. 8 show the chipping phenomenon around the indents. Figure 9a, b, and c show a nearly semicircular shaped "chips" (indicated by the arrows and dotted lines) around the indent for three different loads 1, 2, and 2.5 mN, respectively. It can be noted that the chipping around the indents exhibits a geometrical similarity at all the applied loads. The total chipping area around an indent increases as the applied load is increased. The pop-in phenomenon in the load–depth curves generated by cube corner indenter suggests that the crack begins growing at the very early stage of the loading, continues to propagate downward and toward the surface as the loading continues, resulting in a semicircular shaped chip (Fig. 9) when the crack becomes unstable. It can be noted that the SEM image of the Berkovich indents, Fig. 6 in "Nanoindentation hardness" does not show any cracks or chipping around the indents at a load of 0.8 mN, which may be due to relatively lower stress concentration associated with the Berkovich indenter compared to the cube corner indenter. The chipping phenomenon, similar to the one seen in Fig. 9 has also been reported for the monolithic bulk, brittle solids such as soda lime glass, alumina [20, 22], and thin solid films [21, 28] as well, when the critical failure load is achieved with sharper indenters. The nanoindentation fracture toughness (K_{IC}) was calculated using the following expression

$$P_F/h^{3/2} = \beta K_{IC} \quad (5)$$

where h is the chip size measured from the indent center to the outer edge of the semicircular chip in Fig. 9, P_F is the critical load for failure, β is a constant (9.3 ± 1.3) independent of the material [22]. The expression in the Eq. 5 was originally proposed for the monolithic bulk and brittle ceramic materials based on the edge chipping test using Vickers indenter, which can be applied to sharp cube corner indenter as well, because the cracking mechanism and chip geometry resulting from the latter is similar to the former.

The logarithmic plot of critical failure load versus the average chip dimension is presented in Fig. 10. A regression fit with force fit slope of 1.5 was made to determine βK_{IC} value, which gives the K_{IC} value of 0.28 ± 0.03 MPa $m^{1/2}$. It can be noted that the fracture toughness value calculated from the chip dimensions is in good agreement with the value measured by a Vickers indenter (0.27 ± 0.05 MPa $m^{1/2}$) for the cracks oriented along the interface, when the intermetallic hardness (5.18 MPa) obtained from nanoindentation was substituted for that measured by microhardness testing.

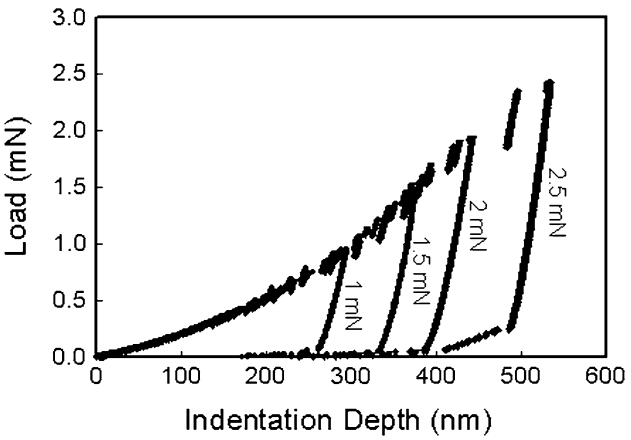

Fig. 8 The load–depth curves for the intermetallic phase at different loads exhibiting "pop-in" phenomenon

Tensile strength and fractography of tensile fracture surfaces

The maximum transverse tensile strength and the failure strain of the weld joints are determined to be 126 MPa and

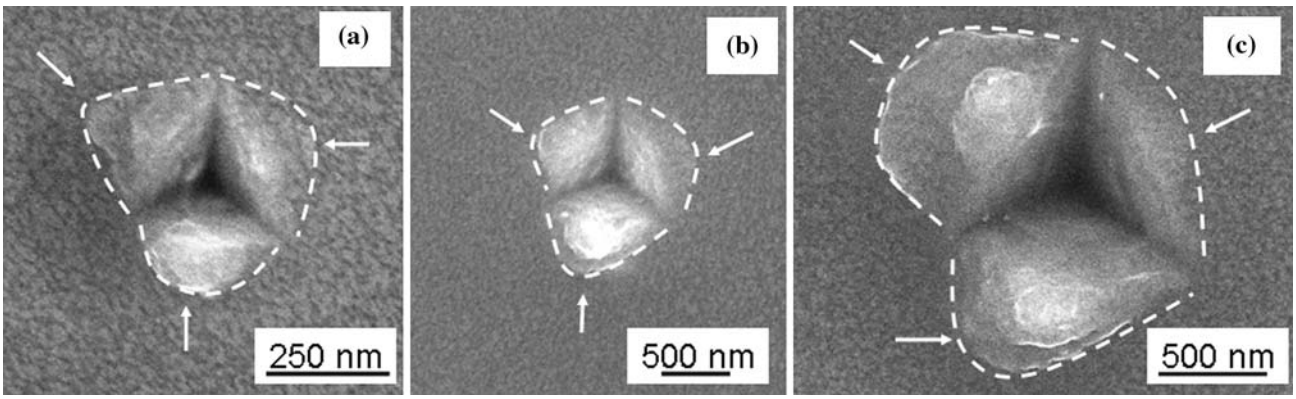

Fig. 9 SEM images show chipping phenomenon. **a**, **b,** and **c** are corresponding to 1, 2, and 2.5 mN applied loads, respectively

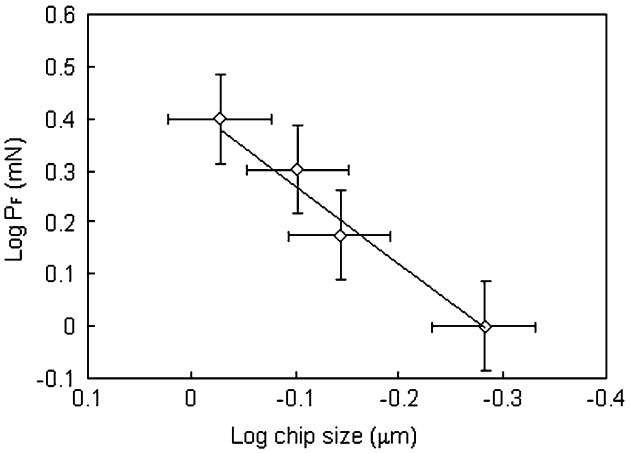

Fig. 10 Log–log plot for the critical failure load versus average chip size

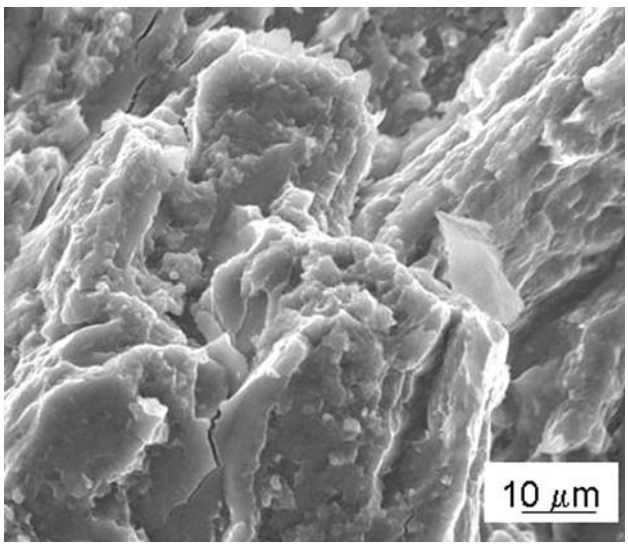

Fig. 11 Secondary electron SEM image of the Al side tensile fracture surface showing brittle fracture with microcracks

1%, respectively. The base materials tensile strength and the elongation are 185, 310 MPa and 12, 10%, for Al and Mg alloys respectively. The maximum weld transverse tensile strength is about 68% of the 6063-T5 Al base metal, however, the ductility of the weld joint is relatively very low compared to the base materials. The presence of an intermetallic layer at the interface has resulted in a brittle failure of the weld joints with virtually nil ductility. The fracture surfaces of the weld joints exhibit brittle failure. Figure 11 shows the fractograph of the Al side tensile fracture surface, showing a completely brittle fracture with microcracks.

X-ray diffraction of tensile fracture surfaces

Figure 12 shows the X-ray diffraction patterns for the Al (a) and Mg (b) sides' tensile fracture surfaces of a weld joint produced using a rotational speed of 1400 rpm, welding speed of 3.38 mm s^{-1} and a z-force of 14.4 kN. The spectra show the peaks of Al_3Mg_2 and $Al_{12}Mg_{17}$ type intermetallic compounds along with the peaks from Al and Mg matrices for both sides of the fracture surfaces, indicating substantial mixing of the base materials during welding (similar peaks were observed on the other weld joints fracture surfaces as well). Similar results have been observed by Chen and Nakata [12] on the Al–Mg lap welds.

Conclusion

In summary, 6063 aluminum and AZ31B magnesium alloys were joined by the FSW process. The weld joint interface contains a narrow intermetallic layer of few micro meters thick along the entire interface length. The intermetallic layer is composed of Al_3Mg_2 and $Al_{12}Mg_{17}$ type intermetallic compounds, characterized by X-ray diffraction and energy dispersive spectroscopy. The intermetallic layer on the as-welded interface exhibits different hardness

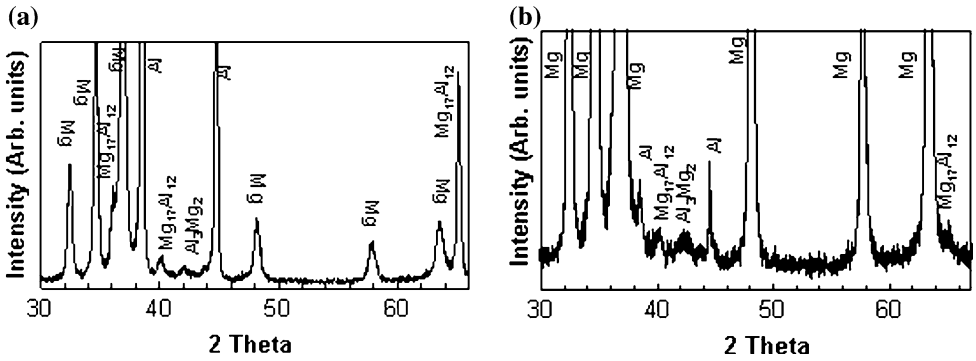

Fig. 12 XRD spectra for the tensile fracture surfaces of Al (**a**) and Mg (**b**) sides

values, 1.56, 3.63, and 5.18 GPa determined by Vickers, Knoop and nanoindentation methods, regardless, the maximum hardness was observed at the weld interface. The chipping phenomenon of the intermetallic layer resulting from cube corner indentation provides a simple means of evaluating the fracture toughness (K_{IC}). The fracture toughness values determined by both Vickers and nanoindentation methods are very low; on the order of soda lime glass and alumina ceramic, which caused the brittle failure of the weld joint. X-ray diffraction and fractography results on the tensile fracture surfaces suggest that the failure of the Al–Mg dissimilar weld joints occur through the brittle intermetallic layer present at the interface.

Acknowledgements The authors acknowledge the financial support of the Center for Friction Stir Processing which is a National Science Foundation I/UCRC supported by Grant No. EEC-0437341. The authors thank Dr. Wei Tang and Daniel Wilhelm, Department of Mechanical Engineering, University of South Carolina, Columbia, SC, USA for their help in preparing the weld joints.

References

1. Reynolds AP (2000) Sci Technol Weld Joining 5(2):120
2. Long T, Tang W, Reynolds AP (2007) Sci Technol Weld Joining 12(4):311
3. Zhang Z (2008) J Mater Sci 43:5867. doi:10.1007/s10853-008-2865-x
4. Khandkar MZH, Khan AJ, Reynolds AP (2003) Sci Technol Weld Joining 8(3):165
5. Zhang Z, Chen JT (2008) J Mater Sci 43:222. doi:10.1007/s10853-007-2129-1
6. Afrin N, Chen DL, Cao X, Jahazi M (2008) Mater Sci Eng A 472:179
7. Commin L, Dumont M, Masse JE, Barrallier L (2009) Acta Mater 57:326
8. Esparza JA, Davis WC, Murr LE (2003) J Mater Sci 38:941. doi:10.1023/A:1022321107957
9. Park SHC, Sato YS, Kokawa H (2003) J Mater Sci 38:4379. doi:10.1023/A:1026351619636
10. Lee CY, Lee WB, Kim JW, Cho DH, Yeon YM, Jung SB (2008) J Mater Sci 43:3296. doi:10.1007/s10853-008-2525-1
11. Somasekharan AC, Murr LE (2006) J Mater Sci 41:5365. doi:10.1007/s10853-006-0342-y
12. Chen YC, Nakata K (2008) Scripta Mater 58:433
13. McLean AA, Powell GLF, Brown IH, Linton VM (2003) Sci Technol Weld Joining 8(6):462
14. Borrisutthekul R, Yachi T, Miyashita Y, Mutoh Y (2007) Mater Sci Eng A 467:108
15. Liming L, Shengxi W, Limin Z (2008) Mater Sci Eng A 476:206
16. Gerlich A, Yamamoto M, North TH (2008) J Mater Sci 43:2. doi:10.1007/s10853-007-1791-7
17. Gerlich A, Su P, North TH (2005) Sci Technol Weld Joining 10(6):647
18. Somasekharan AC, Murr LE (2004) Mater Charact 52:49
19. Sato YS, Park SHC, Michiuchi M, Kokawa M (2004) Scripta Mater 50:1233
20. Morrel J, Gant AJ (2001) Int J Refract Met Hard Mater 19:293
21. Li XD, Bhushan B (1998) Thin solid Films 315:214
22. Chai H, Lawn BR (2007) Acta Mater 55:2555
23. Bailey SJ, Baldini NC (2007) Annual Book of ASTM Standards. ASTM International, PA, USA
24. Oliver WC, Pharr GM (1992) J Mater Res 7:1564
25. Singh D, Suryanarayana C, Mertus L, Chen RH (2003) Intermetallics 11:373
26. Gault C, Dauger A, Boch P (1977) Phys Status Solidi A 43:625
27. Li XD, Bhushan B (2001) Thin Solid Films 398:313
28. Li XD, Bhushan B (1999) Thin Solid Films 355:330